Journal of
Materials Chemistry C

ROYAL SOCIETY
OF CHEMISTRY

PAPER

View Article Online
View Journal

Check for updates

Cite this: DOI: 10.1039/d6tc00820h

Energy transfer mediated Rabi splitting in Ag@CsPbCl$_3$ nanohybrids

Abhishek Kumar, Eeshani Bora and Tushar Debnath *

Received 15th March 2026,
Accepted 21st May 2026

DOI: 10.1039/d6tc00820h

rsc.li/materials-c

We report a strong exciton (semiconductor)–plasmon (metal) coupling in colloidal Ag@CsPbCl$_3$ nanohybrids, leading to the emergence of new hybrid states, known as plexcitons. Here, we systematically tuned the energy separation between these hybrid states at zero-detuning energy, the so-called Rabi splitting, apparent from the simultaneous blue and red shift of the exciton and plasmon resonances, respectively. We observe an extremely large Rabi splitting from the absorption measurement, reaching a value as high as 316 meV. The plexciton energies are modelled using a dissipative coupled-oscillator framework, revealing collective coupling strengths that place the system in both the real and strong coupling regimes. We further establish an active energy transfer process between the CsPbCl$_3$ excitons and Ag plasmons, which underlies the observed strong coupling. The pronounced Rabi splitting observed in colloidal metal–semiconductor nanohybrids establishes a foundation for advancing non-linear plasmonic technologies.

Introduction

The superposition of quantum emitters and surface plasmon polaritons greatly enhances the electromagnetic field strengths by concentrating light–matter interaction at the nanoscale.[1,2] The coupling between these two modes leads to the emergence of two distinct regimes. The interaction in the weak coupling regime partially modifies the radiative decay of the electronic excitations, while the mode frequencies are slightly altered.[3] In contrast, when the interaction between these modes is very strong, it leads to significant changes in the emission properties. In the strong coupling regime, the initial wavefunctions of the excitations and optical modes resonate with one another, allowing for coherent energy exchange. The interaction is so intense that it causes mixing and frequency repulsion between the two states, leading to the formation of two hybrid modes known as upper and lower polaritons. At zero-detuning energy, these polaritons are separated in energy by an amount called the Rabi splitting, which quantifies the strength of the light–matter interaction.[4–7]

The polarization induced by the collective electron oscillations of metal nanostructures leads to the generation of localized surface plasmonic resonances (LSPR).[8] Such plasmons behave like optical resonators and thus may couple with electronic excitations (*i.e.* excitons).[9,10] Strong exciton–plasmon coupling can be achieved using various organic molecules, particularly organic J-aggregates, resulting in the formation of two hybrid resonances (plexcitons), as discussed earlier.[11,12] These plexcitonic states are separated by a large Rabi energy, which is a hallmark of the strong coupling regime.[13] Formation of plexcitons and subsequent Rabi splitting is also observed from the interaction of strong excitons from inorganic semiconductors, such as MoS$_2$, WSe$_2$, CdSe quantum dots (QDs), *etc.*, and LSPR of metal nanostructures, although to a lesser extent.[14–16] In most previous studies, the detuning between exciton and plasmon resonances is varied to observe anti-crossing and determine the Rabi splitting at zero detuning. However, the Rabi splitting energy itself is typically fixed by the intrinsic coupling strength of the system. Systematic control of the Rabi splitting at zero detuning remains relatively limited and therefore represents an important direction for engineering tunable polaritonic systems.

The high absorption cross-section and excellent photoluminescence (PL) properties of QDs make them highly attractive candidates for a wide range of optoelectronic applications, particularly in nanoplasmonic devices.[17] While halide perovskite nanocrystals (NCs) have emerged over the past decade as promising materials for energy and optoelectronic applications,[18,19] there is still limited literature on their coupling with plasmonic metals.[20–22] Coupling with plasmonic metals may significantly broaden the application of perovskite NCs in non-linear plasmonic devices. In our recent study, we explored the plexciton formation in plasmonic perovskite NC systems;[23] however, no Rabi splitting was observed as the detuning energy was non-zero, indicating that further detailed investigation is necessary.

Nano Physical Spectroscopy Group, Department of Chemistry, School of Natural Sciences, Shiv Nadar Institution of Eminence, Delhi NCR, Uttar Pradesh 201314, India. E-mail: tushar.debnath@snu.edu.in, debnathtushar@gmail.com

In this study, we experimentally observe a strong exciton–plasmon coupling, leading to the formation of new hybrid states (*i.e.* plexcitons), in the colloidal Ag incorporated $CsPbCl_3$ NCs (named Ag@CPCl nanohybrids). By varying the Ag-to-$CsPbCl_3$ concentration ratio, we systematically tuned the energy separation between the two hybrid states at zero-detuning energy, the so-called Rabi splitting. We model the observed plexciton energies using a dissipative coupled-oscillator model to quantify the exciton–plasmon coupling strength. Furthermore, steady-state and time-resolved PL measurements were employed to investigate the underlying mechanism of the strong exciton–plasmon coupling, revealing evidence of an active energy transfer process from $CsPbCl_3$ excitons to Ag plasmons.

Experimental

Materials

Cesium carbonate ($CsCO_3$, 99.9%, Spectrochem), lead bromide ($PbBr_2$, 99%, Loba Chemie), lead chloride ($PbCl_2$, ≥99.9%, Sigma-Aldrich), silver nitrate ($AgNO_3$, 99.9%, Sigma-Aldrich), oleylamine (OLA, 98%, Otto Chemie), oleic acid (OA, Sigma-Aldrich, 90%), octadecene (ODE, 90%, Thermo Scientific), *n*-hexane (99%, Finar), and ethanol (Finar) were employed in this study. All reagents were used as received.

Synthesis of Ag nanoparticles

0.17 g of silver nitrate (1 mmol) was mixed with 0.5 mL of oleylamine and 4.5 mL of oleic acid. The mixture was heated at 70 °C for 1.5 hours, then further heated to 180 °C at a rate of 2 °C min^{-1}. After cooling, 10 mL of toluene and 50 mL of ethanol were added to precipitate the nanoparticles. The solution was centrifuged at 8000 rpm for 10 minutes, the supernatant was discarded, and the particles were redispersed in 10 mL hexane.

Synthesis of $CsPbCl_3$ nanoparticles

A stock solution of cesium oleate was prepared by dissolving 0.407 g $CsCO_3$ in 1.25 ml oleic acid (OA) and 20 ml ODE at 120 °C.

Separately, 0.188 mmol $PbCl_2$ was dissolved in 0.5 ml OA, 0.5 ml OLA, and 5 ml ODE at 120 °C for 30 minutes. The temperature was then increased to 165 °C, and 400 µl of the Cs-oleate solution was quickly injected, forming $CsPbCl_3$ nanocrystals. The reaction was immediately quenched using an ice water bath.

The $CsPbCl_3$ NC mixture was centrifuged at 10 000 rpm for 10 min; the supernatant was discarded. The precipitate was redispersed in 2 ml hexane and centrifuged again at 5000 rpm for 5 min. The final supernatant was collected for further use.

Preparation of $PbBr_2$ precursor

0.2 mmol of $PbBr_2$ was dissolved in a mixture of 10 mL hexane, 0.4 mL oleic acid, and 0.4 mL oleylamine by stirring at 100 °C.

Characterization

The morphology of Ag@$CsPbCl_3$ NCs was characterized using TEM and HRTEM (JEOL JEM 2100F with a maximum accelerating voltage of 200 kV). A SHIMADZU UV-2600i UV-vis spectrophotometer was used to measure UV-vis absorption spectra. An Edinburg FS5 fluorescence spectrofluorometer was used to measure PL and time-resolved PL spectra.

Results and discussion

CPCl NCs were synthesized by the colloidal hot injection method and stored in hexane, as reported previously.[24] Ag NPs were synthesized *via* ligand-assisted thermal reduction in oleylamine/oleic acid.[25] The coupled colloidal Ag@CPCl nanohybrids were prepared by mixing Ag NPs and CPCl NCs at various ratios by vortexing at 3000 rpm for 1 min, as shown in Fig. 1a. TEM measurement was performed to understand the morphology of the synthesized CPCl NCs. As shown in Fig. 1b, cubic NCs of ∼10–12 nm size are formed. The lattice fringes are clearly visible in the high-resolution TEM (HRTEM) images in Fig. 1c, indicating high crystallinity of the materials. Furthermore, TEM characterization confirmed the successful formation of Ag@CPCl nanohybrids, as shown in Fig. 1d, where the larger cubes represent CPCl NCs and the black spherical dots on the cubes correspond to Ag NPs. Additionally, the HRTEM image in Fig. 1e reveals a distinct darker region of ∼5–6 nm size corresponding to Ag NPs, along with a clear interface between the two components. The HRTEM image depicts the lattice fringes, indicating the formation of a highly crystalline material.

With the successful synthesis and characterization of Ag@CPCl nanohybrids, we then examined their optical properties using UV-vis absorption, PL and time-resolved PL spectroscopy. The UV-vis optical absorption measurements revealed that the pure CPCl NCs show a sharp excitonic resonance at ∼405 nm, typical for these NCs (Fig. 2a). The pure Ag NPs exhibit a broad absorption resonance between 300 and 500 nm with a maximum at ∼410 nm, arising from LSPR (Fig. 2a). The absorption spectrum of Ag@CPCl nanohybrids exhibits characteristic features of both CPCl NCs and Ag NPs, indicating the coexistence of both components, as shown in Fig. S1. While the position of the exciton resonance of CPCl NCs remains unchanged, interestingly, the LSPR peak position of the Ag NPs redshifts to 443 nm, resulting in overall broadening of the absorption spectrum (Fig. S1).

To understand if the shift in the plasmon peak position from 410 nm to 443 nm (ΔE = 225 meV) is instant or gradual, we further varied the CPCl-to-Ag concentration ratio during the preparation of Ag@CPCl nanohybrids, which may provide important insight into the extent of exciton-to-plasmon interaction. First, we increased the Ag NP concentration in CPCl NCs to decrease the CPCl/Ag ratio. However, the absorption peak positions of excitons and plasmons in different Ag@CPCl nanohybrids remained unchanged, although the absorbance due to plasmon resonance gradually increased, suggesting an

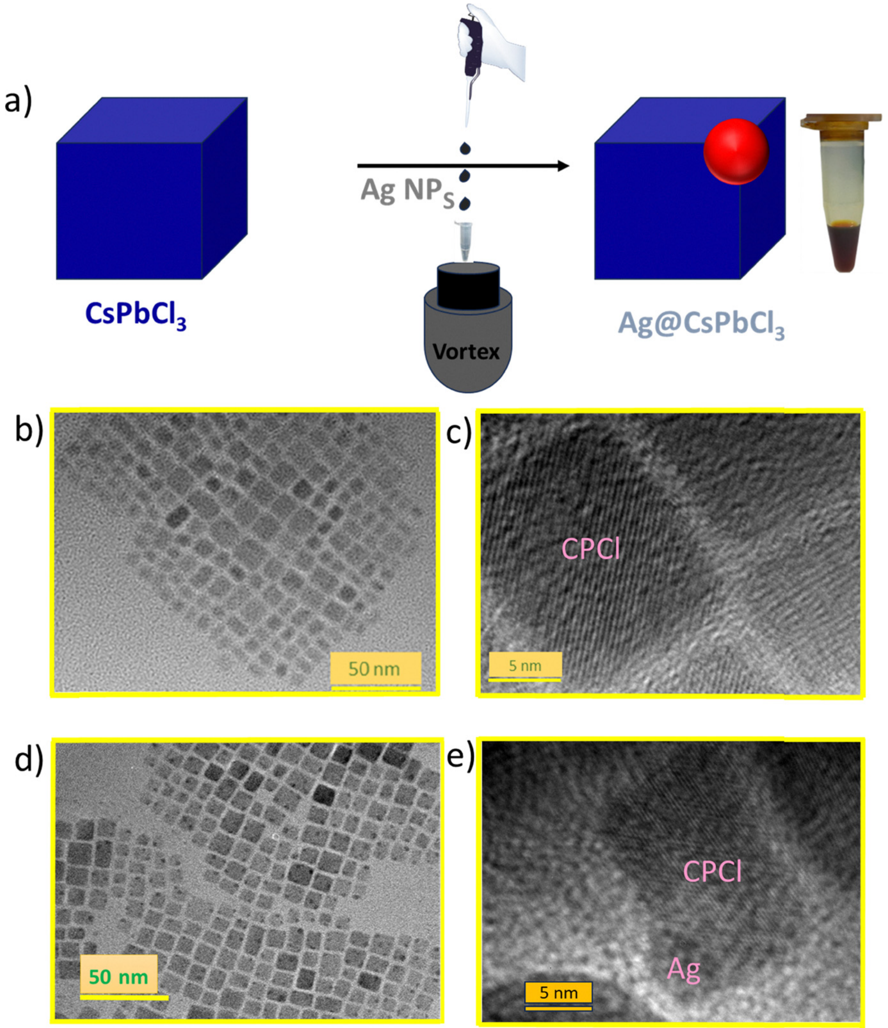

Fig. 1 (a) Schematic illustration of the synthetic procedure of Ag@CPCl NCs. (b) TEM and (c) HRTEM images of CPCl NCs. (d) TEM and (e) HRTEM images of Ag@CPCl NCs.

increase in the exciton-to-plasmon coupling. Then we increased the CPCl/Ag ratio by increasing the proportion of CPCl NCs while the amount of Ag NPs constant (as in Fig. 2a) to prepare a series of Ag@CPCl nanohybrids (see Fig. 2b). To our surprise, increasing the CPCl/Ag ratio by increasing the concentration of CPCl NCs resulted in splitting of the plasmon resonance into two peaks (inset of Fig. 2a). At a low CPCl concentration of ∼6.9 nM, where the exciton interaction is less, the plasmon resonance at 410 nm split into one red-shifted peak at 438 nm and one blue-shifted peak at 405 nm. Upon increasing the concentration of CPCl NCs, the red and blue shifts of the respective peaks continued up to 11.4 nM CPCl concentration, where the plasmon-dominated red-shifted peak settled at 443 nm and the exciton-dominated blue-shifted peak settled at 400 nm due to enhanced exciton–plasmon interaction. No further shift in the respective peaks was observed upon further increasing the CPCl/Ag ratio. It can be seen that the shift of the high energy peak (exciton dominated) to the blue region occurs to a lesser extent compared to the plasmon red shift.

The excitonic resonance of CPCl NCs gradually shifts to shorter (blue) wavelengths, whereas the plasmonic resonance of Ag NPs shifts to longer (red) wavelengths, reflecting their opposite responses in the Ag@CPCl nanohybrids is further depicted in Fig. 2c (and Fig. S2) *via* probing the spectral evolution of excitonic and plasmonic dominated resonances. A maximum energy splitting of 316 meV is observed between the CPCl exciton and Ag plasmons at zero detuning energy (*i.e.* at 410 nm) between the two resonances. Interestingly, the splitting decreases sharply with increasing Ag–$CsPbCl_3$ separation, underscoring the strong distance dependence of exciton–plasmon coupling. While an instantaneous plasmon shift is observed upon the formation of Ag@$CsPbCl_3$ prior to dilution as depicted in Fig. 2b, a delayed (∼50 min) shift is observed when Ag is added after dilution of $CsPbCl_3$, as shown in Fig. S3. This is attributed to slow diffusion and gradual reduction of separation, highlighting the critical role of interfacial chemistry in enabling close proximity and hybrid structure formation.

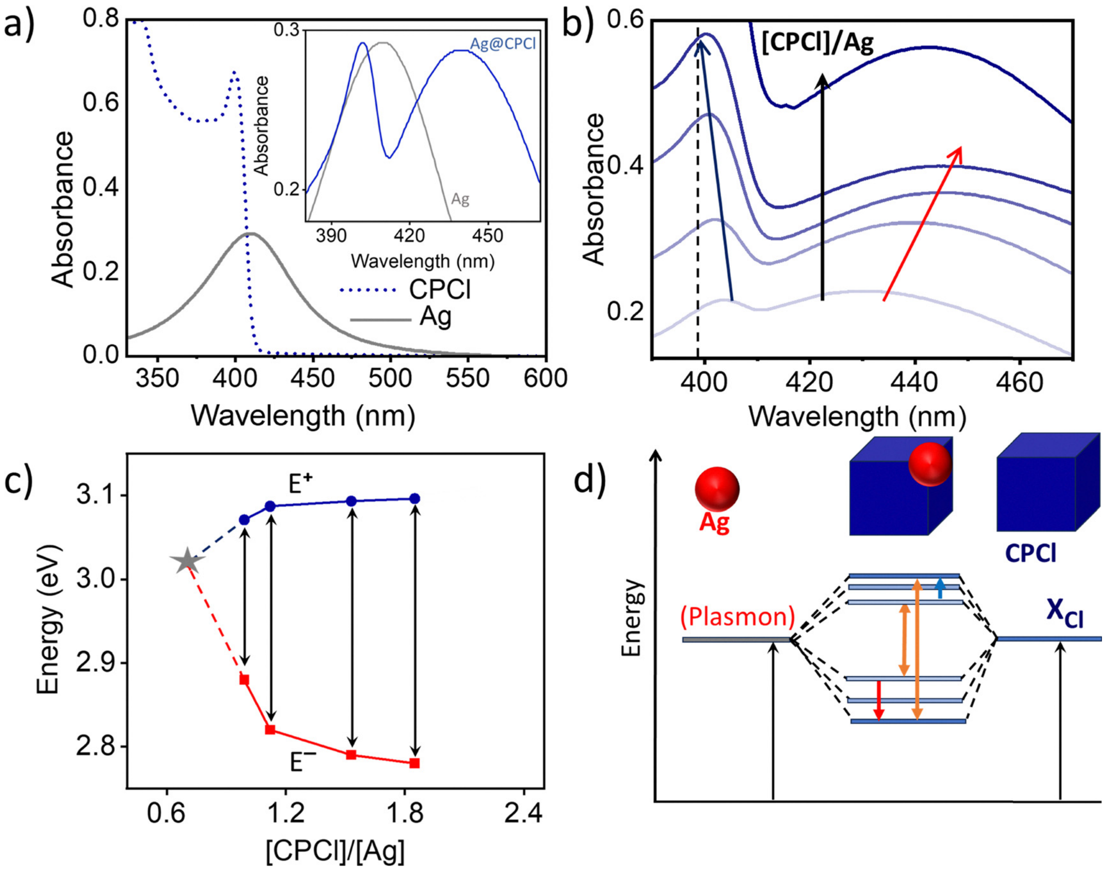

Fig. 2 (a) UV-vis absorption spectra of CPCl NCs and Ag NPs. Inset: UV-vis absorption spectrum of Ag@CPCl NCs for [CPCl] = 6.9 nM and [Ag] = 6.2 nM, *i.e.* [CPCl]/[Ag] = 1.112, along with absorption spectrum of Ag NPs. (b) Magnified view of the UV-vis absorption spectrum of several Ag@CPCl NCs with increasing CPCl concentration at a constant concentration of Ag NPs (*i.e.* varying CPCl-to-Ag ratios). (c) The shift in the upper (E_+) and lower (E_-) plexciton peak positions as a function of the CPCl-to-Ag concentration ratio. The 'star' symbol represents the zero-detuning energy. (d) The energetics of exciton–plasmon interaction in Ag@CPCl NCs with varying CPCl-to-Ag ratios.

Fig. 2d presents the observed optical properties in terms of the energy diagram of Ag@CPCl nanohybrids at various CPCl/Ag ratios by increasing the CPCl NC concentration. With increasing CPCl NC concentration, the excitonic energy gradually shifts toward higher energies (shown by the blue arrow), while the plasmonic energy moves toward lower energies (depicted with the red arrow). In effect, the energy splitting between the exciton and plasmon increases systematically, depicted by orange arrows. The opposite shifts of the excitonic and plasmonic resonances were observed in the earlier studies, revealing the modification of the energy states due to the formation of plexcitons *via* exciton–plasmon coupling through charge-transfer and local-field effects.[26] In most previous studies, plexcitons are formed when excitons from organic J-aggregates interact with the collective electron oscillations in metallic nanostructures.[12] The presence of very high coupling strength in such molecular aggregates enables efficient hybridization between exciton and plasmon resonances, which manifests as an energy splitting between the resulting hybrid states and is commonly referred to as Rabi splitting at zero-detuning energy. While Rabi splitting as large as 450 meV has been experimentally observed in plexcitons formed between organic molecules and plasmonic nanostructures,[27] those involving inorganic semiconductors and plasmonic materials typically exhibit lower splitting, ranging from 100 to 300 meV.[16,28] Our observations of simultaneous blue and red shifts of exciton and plasmon resonances in Ag@CPCl nanohybrids at zero-detuning energy indicate the existence of a strong coupling regime, evidenced by large Rabi splitting into upper and lower polaritonic states, and show a strong CPCl/Ag ratio dependence (Fig. 3a). The maximum splitting observed (Ω = 316 meV) in the developed plasmonic perovskite nanohybrids is thus one of the highest experimental Rabi splittings involving inorganic semiconductor NCs and plasmonic nanomaterials.

To model the observed exciton–plasmon interaction, we consider a dissipative coupled-oscillator model to describe the strong nature of the exciton–plasmon coupling in the Ag@CPCl system. The dependence of the collective exciton–plasmon coupling strength on the number of excitons was theoretically predicted by Rossi *et al.* using excitonic benzene and plasmonic Al particles.[29] The collective coupling strength follows the equation:

$$g_c = \sqrt{N}\mu E_{vac} \tag{1}$$

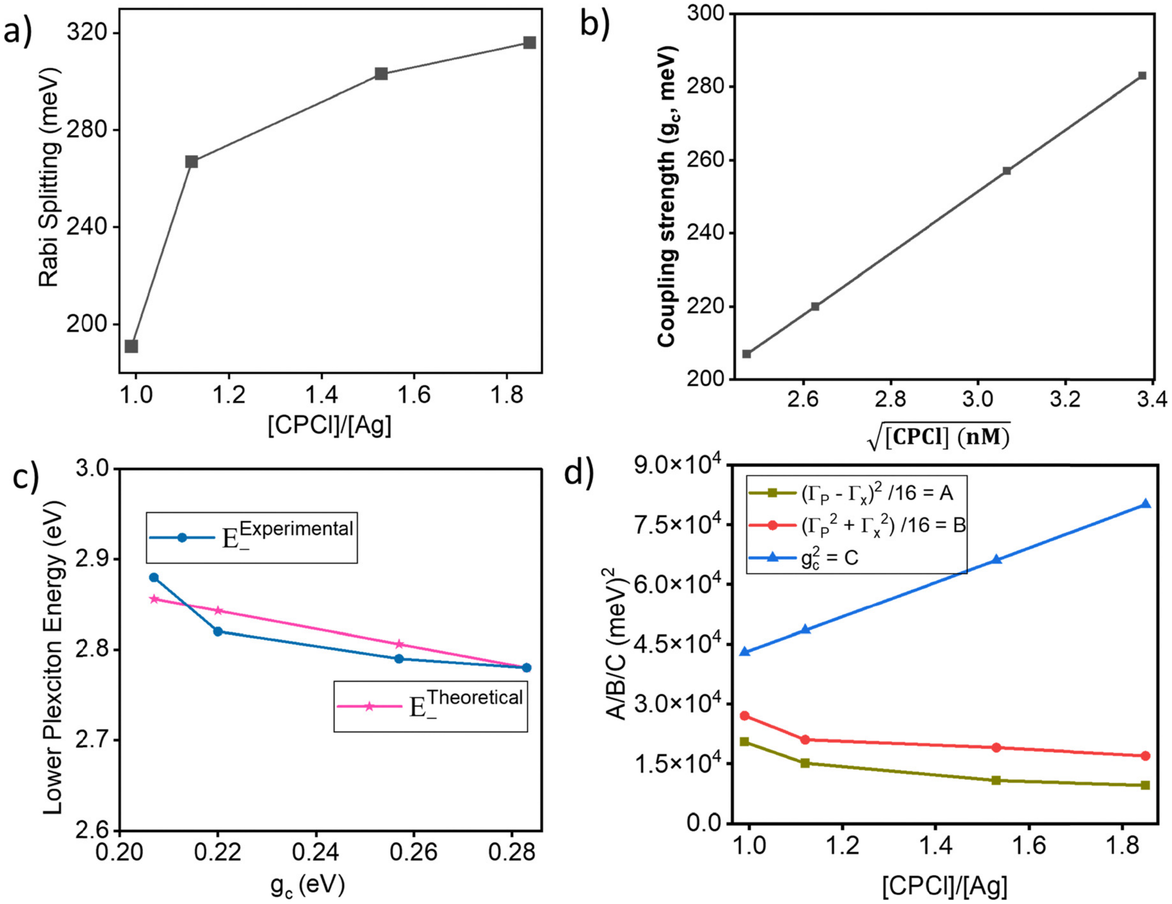

Fig. 3 (a) The plot of experimental Rabi splitting (in meV) with respect to the [CPCl]/[Ag] ratio. (b) The plot of collective coherent coupling strength (in meV) with respect to the concentration of CPCl NCs. (c) Comparison of the theoretical and experimental lower plexciton energies with respect to collective coupling strengths (in eV). (d) Plot showing the two threshold criteria for the real and strong coupling conditions.

Here, N is the effective number of excitons coupled to the plasmon mode, μ is the transition dipole moment and E_{vac} signifies the vacuum electric field. Eqn (1) immediately follows $g_c \propto \sqrt{C}$, where C is the concentration of the CPCl solution. Eqn (1) further provides the single exciton ($N = 1$) coupling strength, which can be written as $g_0 = \mu E_{\mathrm{vac}}$. Furthermore, the system is governed by a non-Hermitian (open) Hamiltonian operator, whose diagonal elements correspond to the damped energies of the uncoupled exciton (E_x) and plasmon (E_p) modes, while the off-diagonal elements represent the coupling strength g_c between them, as shown below:

$$\hat{H} = \begin{pmatrix} E_x - \dfrac{i\Gamma_X}{2} & g_c \\ g_c & E_p - \dfrac{i\Gamma_P}{2} \end{pmatrix} = \begin{pmatrix} \widetilde{E_x} & g_c \\ g_c & \widetilde{E_p} \end{pmatrix} \qquad (2)$$

This Hamiltonian acts on a superposition state of the plasmon and exciton modes:

$$|\psi\rangle = a|x\rangle + b|p\rangle \qquad (3)$$

The resulting hybrid eigenstates (plexcitons) are characterized by the Hopfield coefficients a and b, which quantify the excitonic and plasmonic fractions of the plexciton, respectively, and satisfy the normalization condition $|a^2| + |b^2| = 1$.[30,31] The energy of each of the coupled eigenstates (plexcitons) is then followed by solving the Schrodinger equation that can be expressed as follows, where E_+ and E_- correspond to the upper and lower plexcitons, respectively:

$$E_\pm = \frac{\widetilde{E_x} + \widetilde{E_p}}{2} \pm \sqrt{g_c^2 + \frac{\left(\widetilde{E_x} - \widetilde{E_p}\right)^2}{4}} \qquad (4)$$

The experimental lower plexciton (E_-) can be best fitted using the above energy expression by considering the single exciton coupling strength (normalized with respect to the added CPCl concentration) of $g_0 = 0.084\ \mathrm{eV}\ \sqrt{\mathrm{nM}^{-1}}$. The corresponding collective coupling strength at different CPCl NC concentrations is shown in Fig. 3b, which shows an increase in the g_c value with increasing CPCl concentration. Here, the observed splitting scales as $\Omega \propto \sqrt{N}$ (Fig. 3a and b), which is a signature of the Rabi splitting phenomenon. Using the g_c values, we calculated the lower plexciton energies (theoretical) using eqn (4), which matches the experimental lower plexciton energies up to the first decimal place at all concentration ratios, as depicted in Fig. 3c. Here, we probed the lower plexciton only, as the upper plexciton branch overlaps strongly with the $CsPbCl_3$ exciton resonance and thus exhibits a deviation from the coupled oscillator model, as reported previously.[31]

Now, we aim to understand whether the observed collective coupling strength g_c is real and/or strong. To this end, we need to quantify two threshold criteria. The first criterion arises from the reduced form of the Rabi splitting, which is defined as

$$\Omega = E_+ - E_-$$
$$\Omega = 2\sqrt{{g_c}^2 - \frac{(\Gamma_P - \Gamma_X)^2}{16}} \tag{5}$$

Eqn (5) immediately follows the existence of real hybrid eigenmodes, which must satisfy the inequality:

$$ {g_c}^2 > \frac{(\Gamma_P - \Gamma_X)^2}{16} = A \tag{6}$$

The second threshold criterion corresponds to the strong-coupling regime, which must satisfy the following inequality:

$$ {g_c}^2 > \frac{(\Gamma_P + \Gamma_X)^2}{16} = B \tag{7}$$

which means that the coherent plasmon–exciton exchange rate surpasses the damping rate of bare plasmons and excitons.[30] Fig. 3d shows that the calculated collective coupling strengths at all studied sample concentrations lie above both threshold criteria, indicating that the system operates in the real and strong coupling regimes across the entire investigated concentration range, thus confirming true plexciton behaviour. This accounts for the observation of an exceptionally large Rabi splitting of Ω = 316 meV in the Ag@CPCl system.

The polaritonic nature of the splitting was further confirmed by the anti-crossing phenomenon. By tuning the bandgap of $CsPbX_3$ NCs (X = Cl, Br), we varied the plasmon–exciton detuning and observed clear anti-crossing behaviour (Fig. S4), a hallmark of polaritonic splitting.[31] Moreover, the plasmon response of $Ag@CsPb(Cl{:}Br)_3$ shows a negligible spectral shift relative to bare Ag nanoparticles (Fig. S5), consistent with the negligible exciton–plasmon overlap. As both $Ag@CsPbCl_3$ and $Ag@CsPb(Cl{:}Br)_3$ samples were prepared similarly, their dielectric environments were comparable. Therefore, the pronounced spectral shift in $Ag@CsPbCl_3$ (Fig. 2) arises from its polaritonic nature rather than changes in the local environments (such as the refractive index).

In order to understand the underlying mechanism of exciton–plasmon coupling in the Ag incorporated perovskite nanohybrids,

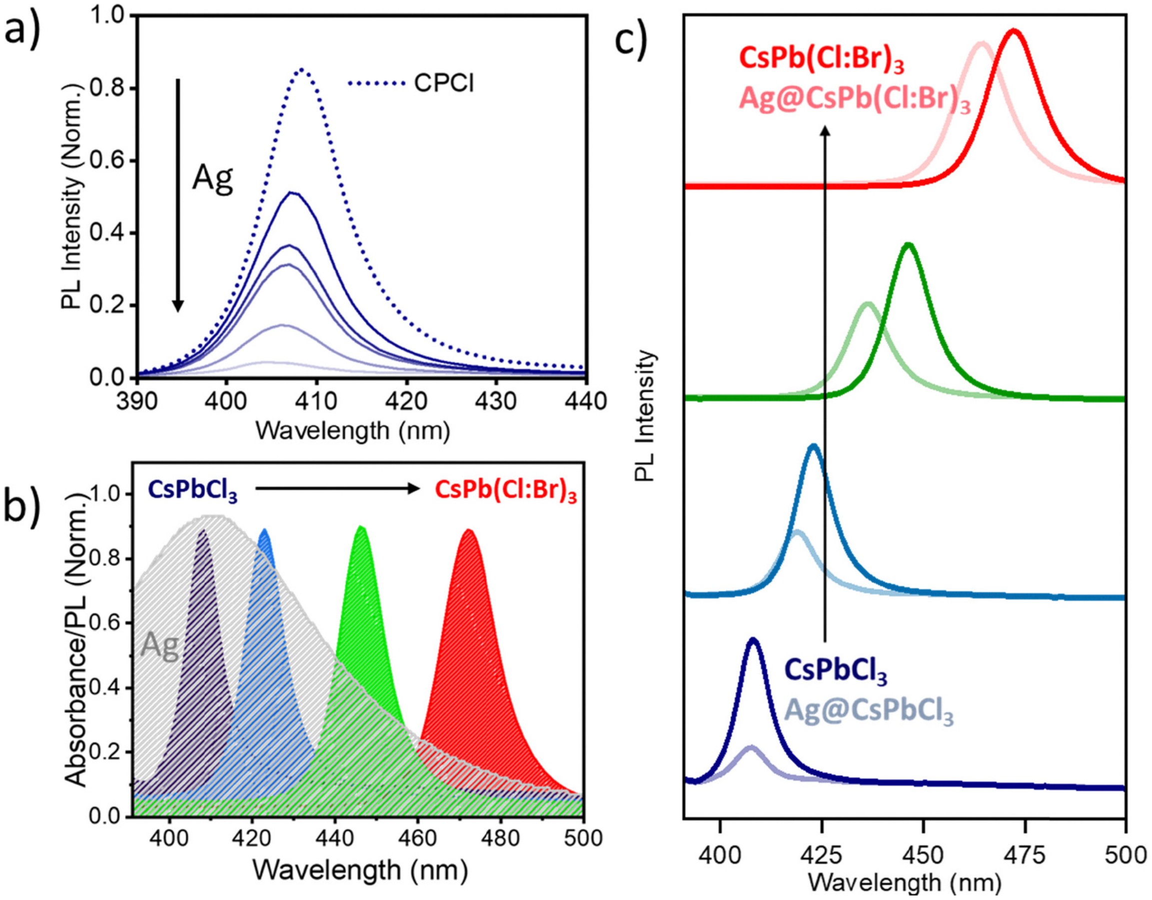

Fig. 4 (a) PL emission spectra of Ag@CPCl NCs with varying CPCl-to-Ag ratios. The PL spectrum of pure CPCl NCs is shown by a dotted line; (b) spectral overlap between the absorption spectrum of Ag NPs and the PL emission spectrum of $CsPb(Cl/Br)_3$ NCs; (c) PL emission spectra of $CsPb(Cl/Br)_3$ NCs without and with Ag NPs.

we performed PL and time-resolved PL measurements on CPCl NCs with increasing Ag NP concentrations to vary the CPCl/Ag ratio. The PL maximum of the pure CPCl NCs appears at 410 nm as shown in Fig. 4a. Upon increasing the Ag NP concentration in order to decrease the CPCl/Ag ratio from 1.85 to 0.99, the PL intensity of the CPCl NCs decreases gradually. A maximum of ~90% PL quenching is observed for the CPCl/Ag ratio of 0.99. We then performed time-resolved PL decay measurement on the CPCl NCs with increasing Ag NP concentrations (Fig. S6). Although the faster lifetime component is limited by the instrument response function (IRF), we observed a progressive decrease in the lifetime of the longer component with decreasing CPCl/Ag ratio. We attribute such a reduction in the PL intensity and lifetime to the CPCl exciton energy transfer to Ag NPs. A strong spectral overlap (see Fig. 4b) between the PL spectrum of CPCl NCs (donor) and the absorption spectrum of the Ag NPs (acceptor) allows an efficient energy transfer between the two components. This can be further evidenced by the controlled PL measurements using Ag incorporated $CsPb(Cl/Br)_3$ with different Cl/Br ratios, resulting in a progressive reduction in the donor–acceptor spectral overlap (due to exciton–plasmon detuning; see Fig. S7a), as shown in Fig. 4b. While the Ag@CPCl nanohybrids show the strongest PL quenching, as the PL of the CPCl NCs shifts to the red region *via* Br exchange, the extent of PL quenching reduces gradually (Fig. 4c and Fig. S7b), supporting the energy transfer mechanism.

It is important to note that PL quenching may also arise from charge transfer and surface trapping, which are very common in these nanocrystals. We noticed that when $CsPbCl_3$ NCs were treated with oleyl ammonium chloride (OAmHCl), a significant PL enhancement *via* surface passivation occurs (Fig. S8a and b).[32] However, Ag@$CsPbCl_3$ prepared from these passivated NCs still showed pronounced PL quenching (Fig. S8c), excluding surface trapping as the primary mechanism for PL quenching. Furthermore, band alignment analysis indicates that electron transfer from photoexcited $CsPbX_3$ (for X = Cl and Br) to Ag is thermodynamically feasible (Fig. S9).[33] Nevertheless, the negligible PL quenching observed for $CsPb(Cl{:}Br)_3$ in the presence of Ag suggests that charge (electron) transfer is not the dominant mechanism, although a minor contribution from electron transfer cannot be neglected. The above result supports the energy transfer from the perovskite NCs to the Ag NPs as the primary underlying mechanism for PL quenching, resulting in strong plexciton formation *via* exciton–plasmon coupling.

Conclusions

Overall, we demonstrate the existence of strong exciton–plasmon coupling in colloidal Ag@CPCl nanohybrids, producing a new hybrid state (plexcitons). By varying the CPCl-to-Ag ratio, we were able to systematically tune the energy separation between the two hybrid states, *i.e.* the Rabi splitting, reaching a value as large as 316 meV. This tuning of the Rabi splitting is evidenced by the simultaneous blue and red shifts of the exciton and plasmon resonances in the optical absorption spectra, respectively. Analysis of the plexciton energies with a dissipative coupled-oscillator model indicates that the collective coupling strengths lie within the real and strong coupling regimes. Using steady-state and time-resolved PL experiments, we demonstrate the energy transfer from the CPCl exciton to the Ag plasmon, enabling the observation of strong exciton–plasmon coupling. The detuning of the donor–acceptor spectral overlap *via* Br exchange to produce Ag@$CP(Cl/Br)_3$ nanohybrids leads to a reduction in PL quenching, supporting the energy transfer mechanism as the underlying mechanism for efficient exciton–plasmon coupling.

Using simple optical absorption spectroscopy, we observed giant Rabi splitting by systematically controlling the system at zero detuning. The measured value represents one of the highest experimental values reported for plasmonic metal–inorganic semiconductor nanohybrids.[32] Furthermore, the Rabi splitting follows the ideal coupled-oscillator model. This work, therefore, establishes a key framework for nanoplasmonic and related nonlinear applications in perovskite systems.

Conflicts of interest

The authors declare no conflicts of interest.

Data availability

Data are available from the corresponding author upon reasonable request.

Supplementary information (SI): details of the calculations, further data on absorption, PL, and lifetime analyses, *etc.* See DOI: https://doi.org/10.1039/d6tc00820h.

Acknowledgements

T. D. acknowledges the Department of Science & Technology (DST) and the Science and Engineering Research Board (SERB) for the Ramanujan Fellowship Award (RJF/2021/000125) and the Core Research Grant (CRG/2023/000519). E. B. thanks the Science and Engineering Research Board (SERB) (project no. RJF/2021/000125) for a fellowship. We thank the School of Natural Sciences, Shiv Nadar Institution of Eminence for instrument support.

References

1 M. Achermann, Exciton—Plasmon Interactions in Metal—Semiconductor Nanostructures, *J. Phys. Chem. Lett.*, 2010, **1**(19), 2837–2843.
2 K. Okamoto, I. Niki, A. Shvartser, Y. Narukawa, T. Mukai and A. Scherer, Surface-plasmon-enhanced light emitters based on InGaN quantum wells, *Nat. Mater.*, 2004, **3**(9), 601–605.
3 D. Kleppner, Inhibited Spontaneous Emission, *Phys. Rev. Lett.*, 1981, **47**(4), 233–236.
4 D. G. Lidzey, D. D. C. Bradley, M. S. Skolnick, T. Virgili, S. Walker and D. M. Whittaker, Strong exciton–photon

coupling in an organic semiconductor microcavity, *Nature*, 1998, **395**(6697), 53–55.

5 C. Weisbuch, M. Nishioka, A. Ishikawa and Y. Arakawa, Observation of the coupled exciton-photon mode splitting in a semiconductor quantum microcavity, *Phys. Rev. Lett.*, 1992, **69**(23), 3314–3317.

6 A. E. Schlather, N. Large, A. S. Urban, P. Nordlander and N. J. Halas, Near-Field Mediated Plexcitonic Coupling and Giant Rabi Splitting in Individual Metallic Dimers, *Nano Lett.*, 2013, **13**(7), 3281–3286.

7 J. Dey, A. Virdi and M. Chandra, Plasmon–Exciton Interaction at the Nanoscale: Silver Is More ''Precious'' than Gold!, *J. Phys. Chem. Lett.*, 2024, **15**(30), 7674–7680.

8 W. L. Barnes, A. Dereux and T. W. Ebbesen, Surface plasmon subwavelength optics, *Nature*, 2003, **424**(6950), 824–830.

9 P. K. Jain, S. Eustis and M. A. El-Sayed, Plasmon Coupling in Nanorod Assemblies: Optical Absorption, Discrete Dipole Approximation Simulation, and Exciton-Coupling Model, *J. Phys. Chem. B*, 2006, **110**(37), 18243–18253.

10 E. Prodan, C. Radloff, N. J. Halas and P. Nordlander, A Hybridization Model for the Plasmon Response of Complex Nanostructures, *Science*, 2003, **302**(5644), 419–422.

11 A. P. Manuel, A. Kirkey, N. Mahdi and K. Shankar, Plexcitonics – fundamental principles and optoelectronic applications, *J. Mater. Chem. C*, 2019, **7**(7), 1821–1853.

12 N. T. Fofang, T.-H. Park, O. Neumann, N. A. Mirin, P. Nordlander and N. J. Halas, Plexcitonic Nanoparticles: Plasmon−Exciton Coupling in Nanoshell−J-Aggregate Complexes, *Nano Lett.*, 2008, **8**(10), 3481–3487.

13 P. Vasa, W. Wang, R. Pomraenke, M. Lammers, M. Maiuri, C. Manzoni, G. Cerullo and C. Lienau, Real-time observation of ultrafast Rabi oscillations between excitons and plasmons in metal nanostructures with J-aggregates, *Nat. Photonics*, 2013, **7**(2), 128–132.

14 W. Liu, B. Lee, C. H. Naylor, H.-S. Ee, J. Park, A. T. C. Johnson and R. Agarwal, Strong Exciton–Plasmon Coupling in MoS2 Coupled with Plasmonic Lattice, *Nano Lett.*, 2016, **16**(2), 1262–1269.

15 M. Wang, A. Krasnok, T. Zhang, L. Scarabelli, H. Liu, Z. Wu, L. M. Liz-Marzán, M. Terrones, A. Alù and Y. Zheng, Tunable Fano Resonance and Plasmon–Exciton Coupling in Single Au Nanotriangles on Monolayer WS2 at Room Temperature, *Adv. Mater.*, 2018, **30**(22), 1705779.

16 H. Wang, H.-Y. Wang, A. Toma, T.-A. Yano, Q.-D. Chen, H.-L. Xu, H.-B. Sun and R. Proietti Zaccaria, Dynamics of Strong Coupling between CdSe Quantum Dots and Surface Plasmon Polaritons in Subwavelength Hole Array, *J. Phys. Chem. Lett.*, 2016, **7**(22), 4648–4654.

17 F. P. G. d Arquer, D. V. Talapin, V. I. Klimov, Y. Arakawa, M. Bayer and E. H. Sargent, Semiconductor quantum dots: Technological progress and future challenges, *Science*, 2021, **373**(6555), eaaz8541.

18 A. Dey, J. Ye, A. De, E. Debroye, S. K. Ha, E. Bladt, A. S. Kshirsagar, Z. Wang, J. Yin, Y. Wang, L. N. Quan, F. Yan, M. Gao, X. Li, J. Shamsi, T. Debnath, M. Cao, M. A. Scheel, S. Kumar, J. A. Steele, M. Gerhard, L. Chouhan, K. Xu, X.-G. Wu, Y. Li, Y. Zhang, A. Dutta, C. Han, I. Vincon, A. L. Rogach, A. Nag, A. Samanta, B. A. Korgel, C.-J. Shih, D. R. Gamelin, D. H. Son, H. Zeng, H. Zhong, H. Sun, H. V. Demir, I. G. Scheblykin, I. Mora-Seró, J. K. Stolarczyk, J. Z. Zhang, J. Feldmann, J. Hofkens, J. M. Luther, J. Pérez-Prieto, L. Li, L. Manna, M. I. Bodnarchuk, M. V. Kovalenko, M. B. J. Roeffaers, N. Pradhan, O. F. Mohammed, O. M. Bakr, P. Yang, P. Müller-Buschbaum, P. V. Kamat, Q. Bao, Q. Zhang, R. Krahne, R. E. Galian, S. D. Stranks, S. Bals, V. Biju, W. A. Tisdale, Y. Yan, R. L. Z. Hoye and L. Polavarapu, State of the Art and Prospects for Halide Perovskite Nanocrystals, *ACS Nano*, 2021, **15**(7), 10775–10981.

19 J. Shamsi, A. S. Urban, M. Imran, L. De Trizio and L. Manna, Metal Halide Perovskite Nanocrystals: Synthesis, Post-Synthesis Modifications, and Their Optical Properties, *Chem. Rev.*, 2019, **119**(5), 3296–3348.

20 S. K. Balakrishnan and P. V. Kamat, Au–$CsPbBr_3$ Hybrid Architecture: Anchoring Gold Nanoparticles on Cubic Perovskite Nanocrystals, *ACS Energy Lett.*, 2017, **2**(1), 88–93.

21 S. Chen, D. Lyu, T. Ling and W. Guo, Reversible modulation of $CsPbBr_3$ perovskite nanocrystal/gold nanoparticle heterostructures, *Chem. Commun.*, 2018, **54**(36), 4605–4608.

22 S. Samanta, S. Paul and T. Debnath, Obtaining Ligand-Free Aqueous Au-Nanoparticles Using Reversible $CsPbBr_3 \leftrightarrow Au@CsPbBr_3$ Nanocrystal Transformation, *Small*, 2024, **20**(19), 2311712.

23 E. Bora, J. P. Das, S. Samanta, A. Kumar and T. Debnath, Plexciton Dynamics in Au-Hybrid $CsPbBr_3$ Perovskite Nanoplatelets, *J. Phys. Chem. Lett.*, 2025, **16**(28), 7134–7139.

24 C. Otero-Martínez, D. García-Lojo, I. Pastoriza-Santos, J. Pérez-Juste and L. Polavarapu, Dimensionality Control of Inorganic and Hybrid Perovskite Nanocrystals by Reaction Temperature: From No-Confinement to 3D and 1D Quantum Confinement, *Angew. Chem., Int. Ed.*, 2021, **60**(51), 26677–26684.

25 J. Park, S. G. Kwon, S. W. Jun, B. H. Kim and T. Hyeon, Large-Scale Synthesis of Ultra-Small-Sized Silver Nanoparticles, *ChemPhysChem*, 2012, **13**(10), 2540–2543.

26 T. V. Shahbazyan, Exciton–Plasmon Energy Exchange Drives the Transition to a Strong Coupling Regime, *Nano Lett.*, 2019, **19**(5), 3273–3279.

27 J. Bellessa, C. Symonds, K. Vynck, A. Lemaitre, A. Brioude, L. Beaur, J. C. Plenet, P. Viste, D. Felbacq, E. Cambril and P. Valvin, Giant Rabi splitting between localized mixed plasmon-exciton states in a two-dimensional array of nanosize metallic disks in an organic semiconductor, *Phys. Rev. B: Condens. Matter Mater. Phys.*, 2009, **80**(3), 033303.

28 D. E. Gómez, K. C. Vernon, P. Mulvaney and T. J. Davis, Surface Plasmon Mediated Strong Exciton−Photon Coupling in Semiconductor Nanocrystals, *Nano Lett.*, 2010, **10**(1), 274–278.

29 T. P. Rossi, T. Shegai, P. Erhart and T. J. Antosiewicz, Strong plasmon-molecule coupling at the nanoscale revealed by first-principles modeling, *Nat. Commun.*, 2019, **10**(1), 3336.

30 E.-M. Roller, C. Argyropoulos, A. Högele, T. Liedl and M. Pilo-Pais, Plasmon–Exciton Coupling Using DNA Templates, *Nano Lett.*, 2016, **16**(9), 5962–5966.

31 G. Beane, B. S. Brown, P. Johns, T. Devkota and G. V. Hartland, Strong Exciton–Plasmon Coupling in Silver Nanowire Nanocavities, *J. Phys. Chem. Lett.*, 2018, **9**(7), 1676–1681.

32 S. H. Shah and T. Debnath, CuInS2-Decorated Perovskite Nanoarchitecture: Halide-Driven Energy and Electron Transfer, *J. Phys. Chem. Lett.*, 2024, **15**(9), 2580–2586.

33 X. Huang, H. Li, C. Zhang, S. Tan, Z. Chen, L. Chen, Z. Lu, X. Wang and M. Xiao, Efficient plasmon-hot electron conversion in Ag–$CsPbBr_3$ hybrid nanocrystals, *Nat. Commun.*, 2019, **10**(1), 1163.